



HAL
open science

In situ study of the evolution of NiFe nanocatalysts in reductive and oxidative environments upon thermal treatments

François Robert, Pierre Lecante, Jean-Sébastien Girardon, Robert Wojcieszak, Éric Marceau, Valérie Briois, Catherine Amiens, Karine Philippot

► To cite this version:

François Robert, Pierre Lecante, Jean-Sébastien Girardon, Robert Wojcieszak, Éric Marceau, et al.. In situ study of the evolution of NiFe nanocatalysts in reductive and oxidative environments upon thermal treatments. *Faraday Discussions*, 2023, 242, pp.353-373. 10.1039/D2FD00095D . hal-03818734

HAL Id: hal-03818734

<https://hal.science/hal-03818734v1>

Submitted on 7 Feb 2023

HAL is a multi-disciplinary open access archive for the deposit and dissemination of scientific research documents, whether they are published or not. The documents may come from teaching and research institutions in France or abroad, or from public or private research centers.

L'archive ouverte pluridisciplinaire **HAL**, est destinée au dépôt et à la diffusion de documents scientifiques de niveau recherche, publiés ou non, émanant des établissements d'enseignement et de recherche français ou étrangers, des laboratoires publics ou privés.

ARTICLE

In situ study of the evolution of NiFe nanocatalysts in reductive and oxidative environments upon thermal treatments

François Robert^{a,b}, Pierre Lecante^c, Jean-Sébastien Girardon^d, Robert Wojcieszak^d, Éric Marceau^{d,*}, Valérie Briois^e, Catherine Amiens^{a,b,*}, and Karine Philippot^{a,b,*}

Received 00th January 20xx,
Accepted 00th January 20xx

DOI: 10.1039/x0xx00000x

Conversion of biomass as a sustainable path to access valuable chemicals and fuels is very attractive for the chemical industry, but catalytic conversions still often rely on the use of noble metals. Sustainability constraints require developing alternative catalysts from abundant and low-cost metals. In this context, NiFe nanoparticles are interesting candidates. In their reduced and supported form, they have been reported to be more active and selective than monometallic Ni in the hydrogenation of the polar functions of organic molecules, and the two metals are very abundant. However, unlike noble metals, Ni and Fe are easily oxidized in ambient conditions, and understanding their transformation in both oxidative and reductive atmospheres is an important though seldom investigated issue to be addressed before their application in catalysis. Three types of NiFe nanoparticles were prepared by an organometallic approach to ensure the formation of ultrasmall nanoparticles (< 3.5nm) of narrow size distribution, controlled composition and chemical order, while working in mild conditions: Ni₂Fe₁ and Ni₁Fe₁, both with a Ni rich core and Fe rich surface, and an alloy of Ni₁Fe₉ composition. Supported systems were obtained by impregnation of silica with the colloidal solution of preformed nanoparticles. Using advanced characterization techniques, such as wide-angle X-ray scattering (WAXS) and X-ray absorption spectroscopy (XAS) in *in situ* conditions, this study reports on the evolution of the chemical order and of the oxidation state of the metals upon exposure to air, hydrogen, and/or increasing temperature, all factors that may affect their degree of reduction and subsequent performance in catalysis. We show that if oxidation readily occurs upon exposure to air, the metals can revert to their initial state upon heating in the presence of H₂ but with a change in structure and chemical ordering.

Introduction

Catalysis holds a pivotal position in the transformation of base molecules into high value-added products for diverse areas of the chemical industry such as energy, textiles, food and health, to name only a few.^{1,2} One of the great challenges of green chemistry³ is to find alternatives to the usual catalytic processes, by replacing non-renewable resources, both at the catalyst and substrate levels, and by limiting resources and energy costs.⁴ Concerning the catalysts, strong efforts aim at developing nanocatalysts in order to gain in active surface area while replacing noble metals by abundant and cheap ones, such as in the first period of transition metals.⁵ Other efforts

focus on the development of recyclable catalysts, making supported systems particularly interesting.⁶ Concerning the starting substrates, biomass offers a large panel of natural and renewable resources to exploit, like sugars that have a key-position in the agri-food sector.^{7,8} For instance, the reduction of the carbonyl groups of sugars allows to access sugar alcohols⁹, also named as polyols, which are suitable molecules in the manufacture of sweeteners.^{10,11} The hydrogenation of sugars into polyols is often carried out on rare and costly noble metals such as ruthenium.^{12,13} A more sustainable substitute can be Raney nickel,¹⁴ which however induces hydrogenolysis side-reactions, owing to its high hydroconversion activity, and is prone to deactivation. Interestingly, the association of Ni and of an abundant metal, Fe, within bimetallic nanoparticles (NPs), has recently shown potential for the hydrogenation of monosaccharides^{15–17} and disaccharides¹⁸, in terms of activity and stability. However, the development of a catalytic formulation requires a proper tuning of the chemical and structural properties of the active phase, and that is not trivial for bimetallic catalysts. The hydrogenation/hydrogenolysis balance is not simply governed by the ratio between the two metals, but also by their degree of interplay, *i.e.* alloyed *vs.* segregated, a crucial point to consider for metals as sensitive

^a CNRS, LCC (Laboratoire de Chimie de Coordination), 205 route de Narbonne, BP 44099, F- 31077 Toulouse Cedex 4, France.

^b Université de Toulouse, UPS, INPT, F-31077 Toulouse Cedex 4, France.

^c CNRS, CEMES (Centre d'Elaboration des Matériaux et d'Etudes Structurales), 29 Rue Jeanne Marvig, BP 4347, F-31055 Toulouse Cedex 4, France.

^d Univ. Lille, CNRS, Centrale Lille, Univ. Artois, UMR 8181 – UCCS – Unité de Catalyse et Chimie du Solide, F-59000 Lille, France

^e Synchrotron SOLEIL, CNRS-UR1, L'Orme des Merisiers, BP48, Saint-Aubin, F-91192 Gif-sur Yvette, France

Electronic Supplementary Information (ESI) available: [details of any supplementary information available should be included here]. See DOI: 10.1039/x0xx00000x

to oxidation as Ni and, even more, Fe.¹⁹ Moreover, as a catalyst is to be recycled, its stability should be studied during its whole cycle of use, including exposure to air and re-activation in H₂, and not only in its as-prepared state.

Accordingly, we have been interested in studying the impact of the chemical environment (oxidative or reductive) on the structural evolution of ultrasmall silica-supported NiFe nanoparticles (3-4 nm in size) that were prepared by an organometallic approach and recently evaluated in the selective aqueous phase hydrogenation of xylose into xylitol.²⁰ The organometallic synthesis method was chosen as it allows an excellent control of size and morphology while working in mild conditions, and the access to supported NPs by simple impregnation of a support with the colloidal solution of the preformed NPs, that thus keep their initial characteristics.^{21,22} Given the oxidability of base metals and the size of the NPs, determining whether the oxidation state of Ni and Fe is significantly and permanently altered by their exposure to air appears fundamental. However, following the structural changes taking place in such small NPs that do not diffract X-rays, is extremely challenging and requires specific strategies. Using advanced characterization techniques, such as wide-angle X-ray scattering (WAXS) and X-ray absorption spectroscopy (XAS) in *in situ* conditions, this study reports on the evolution of the chemical order and oxidation state of the metals upon exposure to air, hydrogen, and/or increasing temperature, as these factors may affect the performance of the NPs in catalysis.

Results

Preparation of the nanomaterials was performed in two steps:

1) hydrogenation of the metal precursors, Ni(COD)₂ (COD=cyclooctadiene) and [Fe[N(SiMe₃)₂]₂]₂, in the appropriate Ni/Fe ratio (2/1, 1/1, 1/9), to produce an homogeneous dispersion of NiFe NPs with mean sizes of 3.4 ± 0.8, 3.1 ± 1.0 and 1.6 ± 0.4 nm, respectively *i.e.* significantly smaller for the iron rich nanomaterial. Transmission electron microscopy (TEM) images and size histograms are displayed on Figures SI1-3;

2) addition of silica to the colloidal solution of NPs, followed by stirring at r.t. The impregnated silica was then collected and washed either in inert conditions to afford reference nanomaterials referred to as NiFe-S, or in air, leading to partially oxidized (*vide infra*) nanomaterials, hereafter referred to as NiFe-S-Ox (see experimental part for details). These nanomaterials were imaged by TEM (Figures 1 and SI1-3), and their structure and extent of oxidation were studied by wide-angle X-ray scattering (WAXS) and/or X-Ray absorption spectroscopy (XAS). Furthermore, the reactivity of the NiFe-S-Ox nanomaterials with respect to H₂ was followed by *in situ* XAS measurements in the 30-530°C temperature range, after which the extent of their reoxidation upon air exposure was checked.

Reference nanomaterials prepared in inert conditions: NiFe-S.

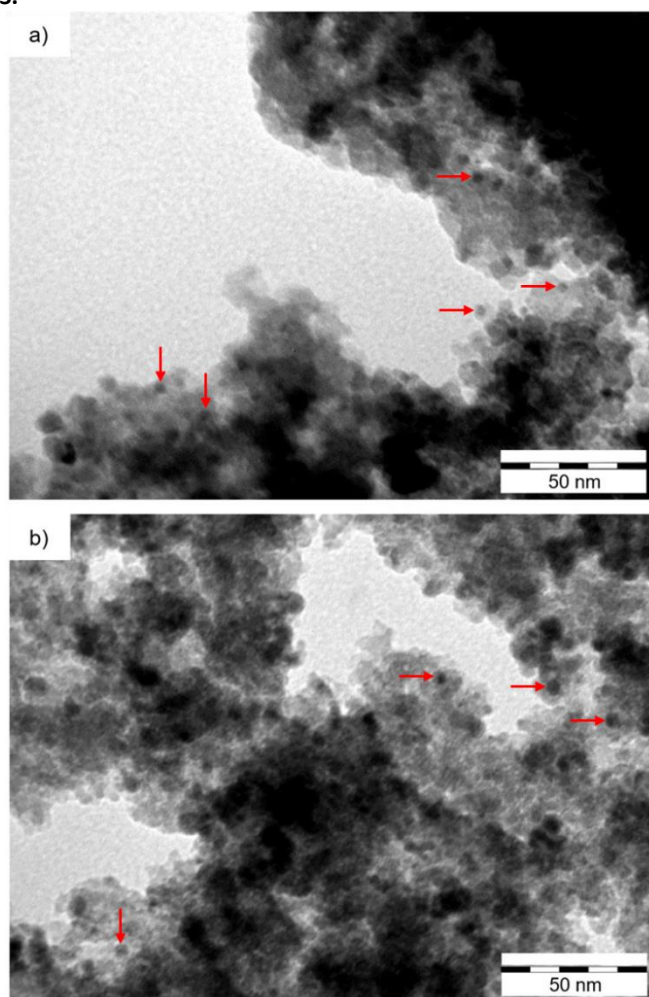


Fig 1: TEM images of a) Ni₂Fe₁-S, and b) Ni₂Fe₁-S-Ox, red arrows pointing some typical NPs.

Analysis by Inductively coupled plasma - optical emission spectroscopy (ICP-OES) evidenced Ni/Fe ratios that matched the initial ratios of Ni and Fe introduced for the synthesis of the NPs (namely Ni_{0.67}Fe_{0.33}, Ni_{0.52}Fe_{0.48} and Ni_{0.10}Fe_{0.90} for Ni₂Fe₁-S, Ni₁Fe₁-S, and Ni₁Fe₉-S).

For all three compositions, dark dots well-dispersed and contrasting from the silica support were observed on conventional TEM images (Figures 1 and SI1-3), that were attributed to the NiFe NPs based on dark field TEM images (e.g. in Fig SI 1b). The limited number of NPs that could be observed with accuracy was not sufficient to draw a size histogram. However, the size of the NiFe NPs that could be measured was found in good agreement with the mean size of their non-supported counterparts, namely 3.4, 3.1 and 1.6 nm for Ni₂Fe₁-S, Ni₁Fe₁-S, and Ni₁Fe₉-S, respectively.

Differences between the three systems also exist in terms of structure. Ni₂Fe₁-S and Ni₁Fe₁-S WAXS diagrams, recorded in air-tight conditions, displayed similar features (Figure 2 a)). No oxide contribution was evidenced. Typical peaks for fcc Ni (note that since the lattice parameters of some iron-poor NiFe alloys are very close to those of pure Ni, WAXS cannot inform

on a limited diffusion of Fe in this fcc core, which cannot be excluded) were observed at 20, 23, 33 and 39°, together with a shoulder on the left side of the main peak (20°) and a peak at *ca.* 36° that are attributed to Fe in a polytetrahedral arrangement. These two features are comparable to those of unsupported Ni₁Fe₁ NPs, reported before.²³ The radial distribution functions (RDF) (Figure 2 b), also match the one of the unsupported Ni₁Fe₁ NPs. A comparison with the RDF from reference fcc Ni shows that some extra peaks and shoulders (for instance at 0.9 nm) can only be explained by the polytetrahedral fraction.

Contrarily, the WAXS data of Ni₁Fe₉-S (Figure 3) evidenced only a fully polytetrahedral arrangement, both in the reciprocal and direct spaces. Again, no oxide contribution was detected. This packing is well documented for Fe NPs^{24–27}, and, to the best of our knowledge, was never observed for Ni NPs. Given the limited amount of Ni in Ni₁Fe₉, this result strits consistent with the formation of an alloy, in which Ni atoms would be diluted into the polytetrahedral Fe arrangement.

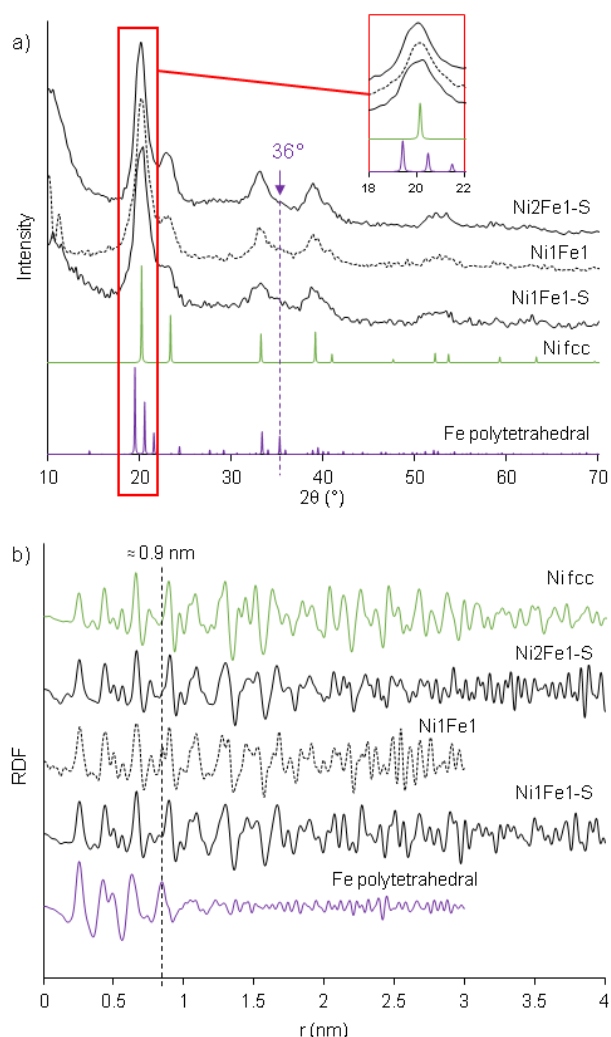


Fig 2: WAXS analysis of Ni₂Fe₁-S and Ni₁Fe₁-S in a) reciprocal space and b) direct space. Ni₁Fe₁ data from²³, fcc Ni and Fe in a polytetrahedral arrangement are included for comparison purposes

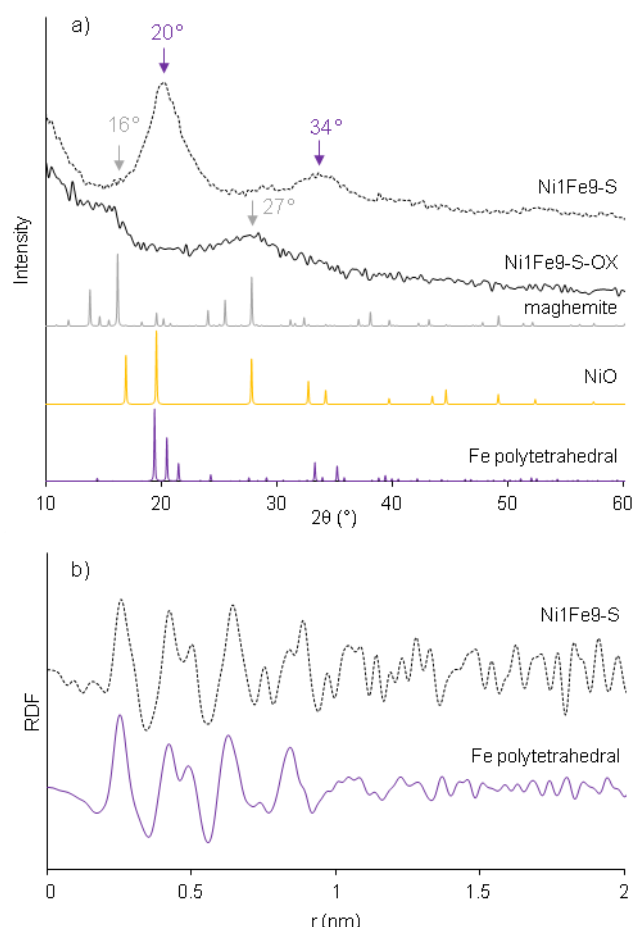


Fig 3: WAXS analysis of Ni₁Fe₉-S in a) reciprocal space and b) direct space.

Air-exposed nanomaterials: NiFe-S-Ox.

Here also, ICP-OES evidenced Ni/Fe ratios that matched the initial ratio of Ni and Fe introduced (namely Ni_{0.66}Fe_{0.34}, Ni_{0.52}Fe_{0.48} and Ni_{0.10}Fe_{0.90} for Ni₂Fe₁-S-Ox, Ni₁Fe₁-S-Ox, and Ni₁Fe₉-S-Ox). The TEM image of Ni₂Fe₁-S-Ox (Figure 1), shows comparable morphology and size to those of Ni₂Fe₁-S prepared in inert conditions. The same holds for Ni₁Fe₁-S-Ox, and Ni₁Fe₉-S-Ox (Figures S1-3).

The three NiFe-S-Ox systems were investigated by WAXS in comparison to NiFe-S ones to determine the effects of exposure to air. Data from fcc Ni, NiO and maghemite were extracted from databases for comparison (Figures 3a and 4). Note that maghemite is used here only as a representative example of iron oxides (such as maghemite, hematite, magnetite...) as 1) it is not possible to distinguish between the different iron oxides structures with our experimental set-up and 2) the highly ordered spinel structure only exists for NPs of larger sizes anyway.

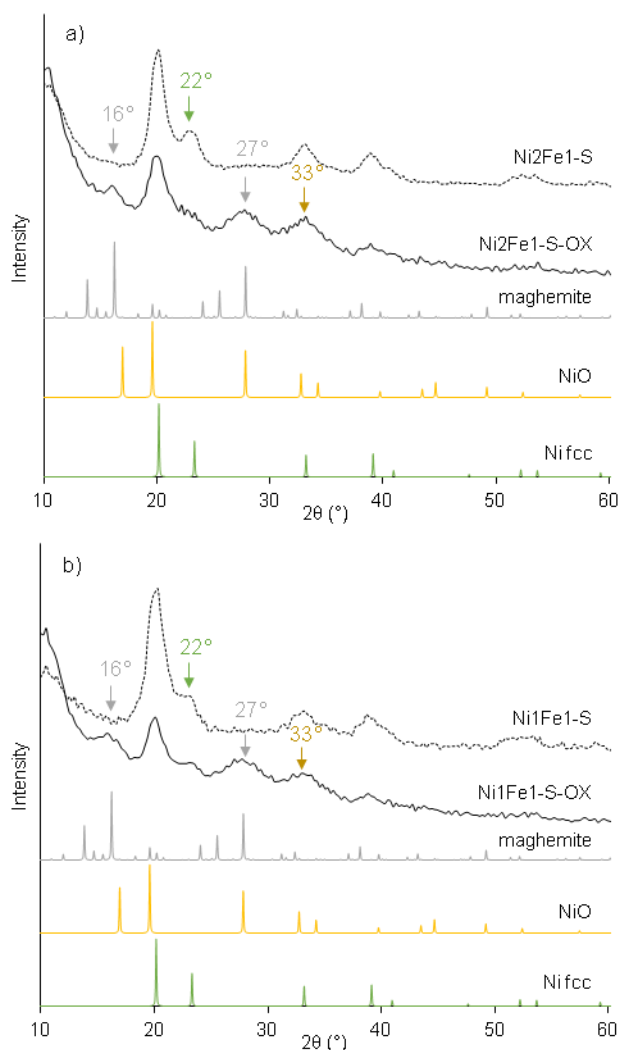


Fig 4: WAXS analysis in reciprocal space of a) Ni₂Fe₁-S-Ox and b) Ni₁Fe₁-S-Ox

In comparison to Ni₂Fe₁-S and Ni₁Fe₁-S, new peaks (at 16° and 27°) are observed for Ni₂Fe₁-S-Ox and Ni₁Fe₁-S-Ox that closely match the maghemite reference peaks, indicating that Fe was oxidized. The decrease in the relative intensity of the peak at 22°, characteristic of fcc Ni, and the enlargement of the peak at ca. 33° also evidence the partial oxidation of Ni into NiO. But comparing the relative intensities of all the peaks suggests that Fe was more oxidized than Ni during air exposure, pointing to the formation of a Fe-rich oxide at the NP surface. It also suggests that a larger fcc Ni core persisted in Ni₂Fe₁-S-Ox than in Ni₁Fe₁-S-Ox (here again, a limited diffusion of Fe in this fcc core cannot be excluded). Contrarily, the WAXS diagram of Ni₁Fe₉-S-Ox (Figure 3a) evidences a full oxidation of the NPs, which could be expected given their smaller size (1.6nm vs. 3.4-3.1nm) and their higher Fe content, Fe being more oxophilic than Ni. As a conclusion, the use of these S-Ox systems in catalysis would require a re-activation under H₂.

In situ study of the reactivity of NiFe-S-Ox in a H₂/He flow as a function of the temperature.

This study was carried out by X-ray absorption spectroscopy at the Fe and Ni K-edges, monitored simultaneously. A measurement was made prior to introducing the gas flow to record the initial state. Then a H₂ (5%)/He flow was passed through the cell (50mL/min) and a temperature ramp was set (5°C/min.; 30-530°C). These conditions were selected based on a previous study on NiFe nanocatalysts prepared by deposition – precipitation with urea (DPU).²⁸ The proportions of the different Fe and Ni species were determined by a multivariate data analysis (see Exp. and SI for details).

Initial state. At the Fe K-edge, a comparison of the XANES spectra with those of standard oxides (Figure SI 4a) suggests a major oxidation of Fe into Fe(III), in line with WAXS results. Besides the first peak arising from the O neighbours, the Fourier transforms (FT) of the EXAFS oscillations display a second peak that is strongly dampened (as the result of local disorder and location of Fe mainly in the surface shell of the NPs) (Figure 5a), precluding any exact identification of the phase formed (maghemite, magnetite or hematite). The intermediate region, visible especially for Ni₂Fe₁-S-Ox (at 2 Å, figure 5a), is an indication of the presence of a small amount of metallic Fe. This suggests the presence of some Fe in the fcc core of the NPs.

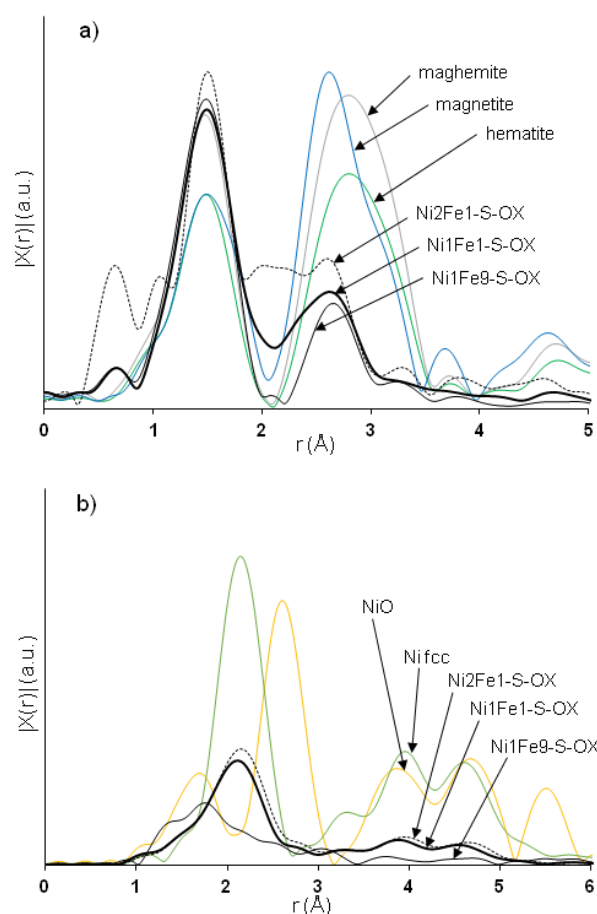


Fig 5: FT of the EXAFS oscillations at a) Fe K and b) Ni K edges

At the Ni K-edge (Fig SI 4b), Ni₂Fe₁-S-Ox and Ni₁Fe₁-S-Ox showed different results than Ni₁Fe₉-S-Ox. For the first two, the pre-edge region (below 8340 eV) still presented a significant contribution from metallic Ni, and the four peaks characteristic of fcc Ni are visible on the FT (Fig 5b), while the XANES spectrum and FT are more reminiscent to those of NiO for Ni₁Fe₉-S-Ox. This is also in line with WAXS results.

Fitting of the EXAFS oscillations and FT for Ni₂Fe₁-S-Ox and Ni₁Fe₁-S-Ox confirms these results (Fig SI 5-6 and Table 1). Coordination numbers were lower than in compact structures as often observed in NPs. At the Fe K-edge, the EXAFS fit pointed to a mainly oxidic environment around Fe(III) (*ca.* 6-7 O at R = 1.96 Å, *ca.* 2-3 Feⁿ⁺ at 2.97-3.02 Å, n=2 or 3) with a minor metallic contribution (*ca.* 1 metallic atom at R = 2.51 Å) which could arise from the dilution of Fe in the NPs fcc core, or from the interface between the Ni-rich core and the Fe oxide shell. At the Ni K-edge, in addition to an oxidic contribution typical of NiO (less prominent for Ni₂Fe₁-S-Ox than for Ni₁Fe₁-S-Ox in accordance with WAXS results), a direct Ni-M (M=Fe or Ni) bond was still present and fitted well with the Ni-Ni bond in fcc Ni (4-5 Ni at R = 2.49 Å). The larger number of metallic neighbours compared with the Fe K-edge confirms that Ni, more abundant than Fe in the core of the NPs, has been significantly protected from oxidation. Fitting of the EXAFS data for the Ni₁Fe₉-S-Ox sample was not satisfactory most probably due to this unusual polytetrahedral structure that comprises a large distribution of distances, and to the small size of the NPs which induces a large proportion of surface atoms and possibly disorder.

It is difficult to rely simply on EXAFS fitting for a quantitative analysis, as it is impaired by a number of parameters too limited to describe mixtures of metal and Feⁿ⁺ oxides that exhibit a variety of interatomic distances, and by the impossibility to distinguish between Ni or Fe metallic neighbours because of the low Z-contrast (the best quality of the fits was reached by selecting Ni atoms only, though this may not reflect the chemical reality). It was thus preferred to quantify the composition of the systems by performing a MCR-ALS analysis based on two components (see next section and Exp. for details); the spectrum of hematite was added to the matrix at the Fe K-edge to better extract the minor metallic component. The analysis led to 93% of Fe(III) oxides (7% Fe(0)) in Ni₂Fe₁-S-Ox, 99% of Fe(III) oxides (1% Fe(0)) in Ni₁Fe₁-S-Ox, and 100% Fe(III) oxides in Ni₁Fe₉-S-Ox. At the Ni K-edge, the contributions were found as *ca.* 60% for Ni(0) (40% Ni(II)) in Ni₂Fe₁-S-Ox and Ni₁Fe₁-S-Ox, but only 34% for Ni(0) (66% Ni(II)) in Ni₁Fe₉-S-Ox (Table 1). The structure of the metallic phases will be discussed in the next section.

Redox phenomena in the presence of H₂ as a function of the temperature. XAS spectra (Fe and Ni K-edges) were next collected during a temperature programmed reduction (TPR) (Figure 6, SI 7-10). The colour gradient from dark blue to red is related to the increasing temperature. At the Ni K-edge, as indicated by the isosbestic points observed in the superimposition of the XAS spectra over the whole temperature range (Figure 6a, SI 7 and 9), MCR-ALS analysis evidenced in each case two spectral components, one

representative of Ni(II) presenting a characteristic intense white line (identical for the three NiFe-S-Ox and very close to NiO), and the other one representative of metallic Ni (Figure SI 11a). Surprisingly, for Ni₂Fe₁-S-Ox and Ni₁Fe₁-S-Ox, an increase of the oxidation degree of Ni was observed in the 30°C-272°C ramp (from dark blue to green), despite the reducing atmosphere. Only above 272°C did Ni reduce to the fully metallic state as evidenced by the global shape and position in energy of the final XANES spectrum. This metallic component displayed a XANES spectrum very close to that of reference fcc Ni, which was confirmed by comparison of the FT. For Ni₁Fe₉-S-Ox, the XANES spectrum of the second component deviated from that of fcc Ni and the FT suggested a polytetrahedral atomic packing²⁶ the position of the first peak is unusually low when compared with fcc Ni, pointing to the existence of short metal-metal distances as in the polytetrahedral structure (Figure SI 11b). This cannot be ascribed to an oxidation of Ni given the low position in energy of the edge, similar to that of fcc Ni.

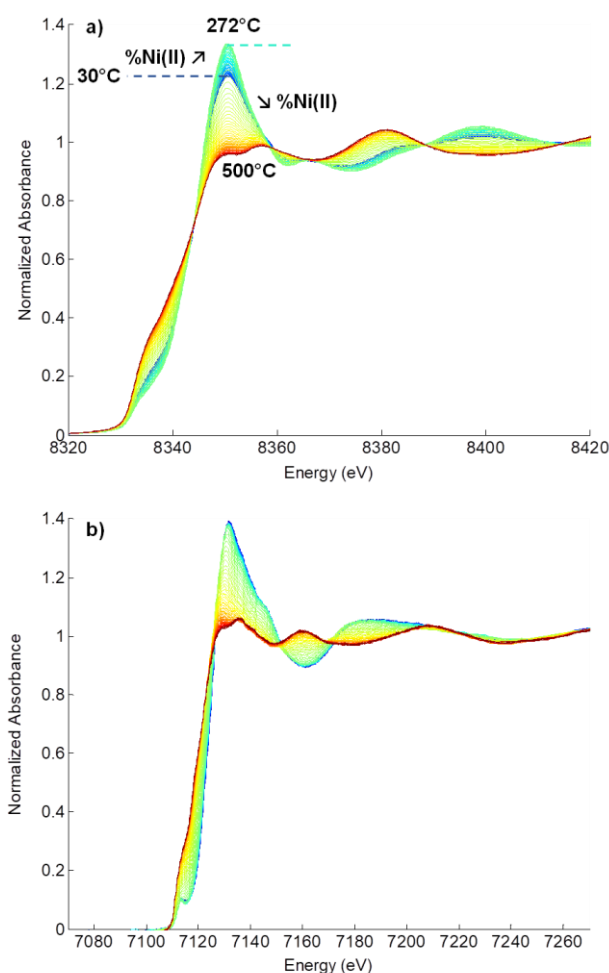


Fig 6: Evolution of the XAS spectra of Ni₂Fe₁-S-Ox under H₂/He flow as a function of temperature a) at Ni K-edge, b) at Fe K-edge. (colour scale from blue: 30°C to red: 530°C; for the sake of clarity only one spectrum over four is drawn).

At the Fe K-edge (Figures 6b, SI 8 and 10), three components were extracted by the MCR-ALS analysis (Figure SI 12). A

comparison of the edge position with standards indicates that the first two represent oxidic species predominantly containing Fe(III) or Fe(II), respectively, and they are similar for the three systems. In contrast, and in accordance with the analysis at the Ni K-edge above, the shape of the XANES region for the third components, corresponding to Fe(0), differs from one system to the other. For Ni₂Fe₁-S-Ox and Ni₁Fe₁-S-Ox, the XANES spectrum and FT of the third component are similar

and close to those of fcc Fe (four characteristic peaks on the FT), while it is closer (but not identical) to that of a polytetrahedral atomic packing for Ni₁Fe₉-S-Ox (Figure SI 12c, d). Qualitatively speaking, the evolution of the spectra is more typical than at the Ni K-edge: the spectra gradually shift to lower energies, and the intensity of the white line decreases when the reduction temperature increases, as one can expect for successive transitions involving Fe(III), Fe(II) and Fe(0).

Table 1. Structural parameters determined from the EXAFS analysis of the spectra recorded at r.t. at the Ni K edge ($E_0 = 8340 \pm 2$ eV, $S_0^2 = 0.77$) and Fe K edge ($E_0 = 7120 \pm 4$ eV, $S_0^2 = 0.72$) before reduction and results from MCR-ALS analysis.

	Backscatterer	N	σ^2 (\AA^2) $\times 10^3$	R (\AA)
Ni K edge				
Ni ₂ Fe ₁ -S-Ox	O	2.2 \pm 0.5	6 \pm 2	2.01 \pm 0.03
	Ni	5 \pm 2	6 \pm 2	2.49 \pm 0.02
	Ni	1.9 \pm 0.6	6 \pm 2	2.98 \pm 0.04
<i>r-factor = 0.00825, $\chi^2 = 451$, $N_{ind} = 10$, $N_{var} = 8$</i>				
MCR-ALS analysis: 40% Ni(II), 60% Ni(0) fcc				
Ni ₁ Fe ₁ -S-Ox	O	2.9 \pm 0.6	6 \pm 2	2.01 \pm 0.03
	Ni	4 \pm 2	6 \pm 2	2.49 \pm 0.02
	Ni	1.7 \pm 0.6	6 \pm 2	2.99 \pm 0.04
<i>r-factor = 0.00914, $\chi^2 = 481$, $N_{ind} = 10$, $N_{var} = 8$</i>				
MCR-ALS analysis: 40% Ni(II), 60% Ni(0) fcc				
Ni ₁ Fe ₉ -S-Ox	MCR-ALS analysis: 66% Ni(II), 34% Ni(0)			
Fe K edge				
Ni ₂ Fe ₁ -S-Ox	O	6 \pm 3	9 \pm 5	1.96 \pm 0.03
	Ni	1.6 \pm 0.9	9 \pm 5	2.51 \pm 0.04
	Fe	2 \pm 2	9 \pm 5	2.97 \pm 0.04
<i>r-factor = 0.01845, $\chi^2 = 2195$, $N_{ind} = 9$, $N_{var} = 8$</i>				
MCR-ALS analysis: 93% Fe(III), 7% Fe(0) fcc				
Ni ₁ Fe ₁ -S-Ox	O	7 \pm 2	12 \pm 3	1.96 \pm 0.02
	Ni	0.9 \pm 0.4	12 \pm 3	2.51 \pm 0.04
	Fe	2.7 \pm 0.9	12 \pm 3	3.02 \pm 0.02
<i>r-factor = 0.00825, $\chi^2 = 653$, $N_{ind} = 9$, $N_{var} = 8$</i>				
MCR-ALS analysis: 99% Fe(III), 1% Fe(0) fcc				
Ni ₁ Fe ₉ -S-Ox	MCR-ALS analysis: 100% Fe(III)			

N: Coordination number; σ : Debye-Waller factor; R: Distance between absorbing atom and neighbours; *r-factor*: reliability factor, which measures the relative misfit with respect to the data; χ^2 : reduced chi-square, which takes into account the uncertainty level in the data, as well as the number of free parameters allowed to vary in the fit. N_{ind} : number of independent variables. N_{var} : number of variables used for the fit. Simulations were done over Δk range = 3.5–11.0 \AA^{-1} for Fe, 3.2–11.5 \AA^{-1} for Ni, and $\Delta R = 1$ –3.4 \AA .

ARTICLE

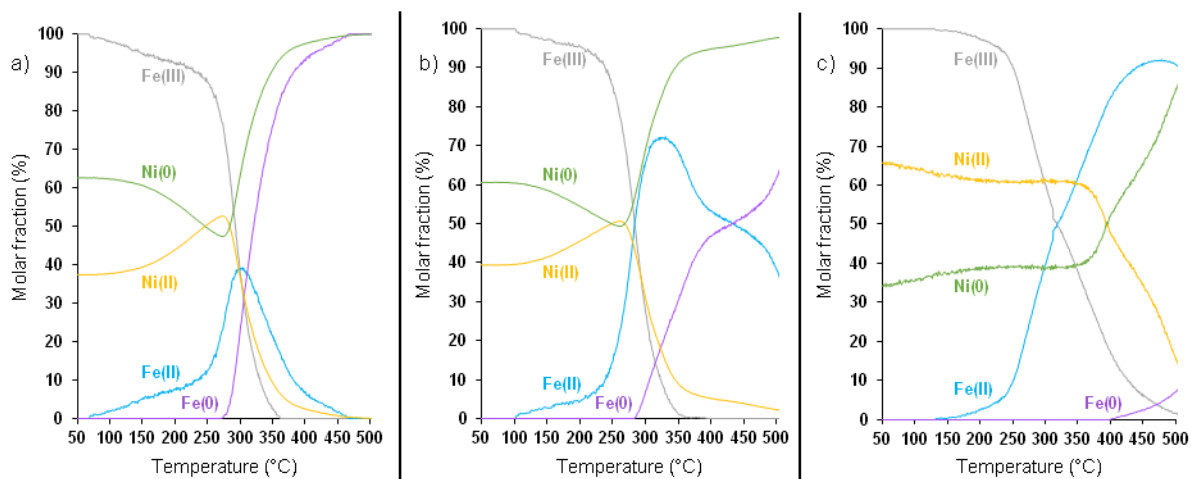


Fig 7: MCR-ALS monitoring of the TPR of a) Ni₂Fe₁-S-Ox, b) Ni₁Fe₁-S-Ox, and c) Ni₁Fe₉-S-Ox (temperature ramp: 5°C/min; reducing conditions: 5% H₂ in He, gas flow: 50 mL min⁻¹).

The relative weights of each contribution to the XANES spectra were determined as a function of temperature (or time) as displayed on Figures 7 and SI 13. Ni₂Fe₁-S-Ox and Ni₁Fe₁-S-Ox presented similar behaviours: above 100°C, the contribution of Ni(II) increases progressively despite the reducing atmosphere, as well as the contribution of Fe(II) (initially absent), at the expense of the contributions of Ni(0) and Fe(III), suggesting that a redox reaction occurs between Fe and Ni at the interface between the reduced core and the oxidic shell. The same phenomenon was observed in a control experiment carried out under pure He for Ni₂Fe₁-S-Ox (Figures SI 14). The simultaneous formation of Ni(0) and Fe(0) was observed above 270°C - 280°C for Ni₂Fe₁-S-Ox and Ni₁Fe₁-S-Ox. Full reduction was achieved in 1h30 (when the temperature reached *ca.* 470°C) for the Ni rich sample Ni₂Fe₁-S-Ox, while it required *ca.* 1h50 more at 520°C for Ni₁Fe₁-S-Ox. The reduced states being described by a fcc structure at Ni and Fe edges based on the shape of their XANES spectra (Figure SI 15) suggests that alloying occurs during the TPR for these two nanomaterials. Reduction of the Fe rich nanomaterial Ni₁Fe₉-S-Ox followed a different pattern (Figure 7). No internal redox event could be evidenced in this case, in agreement with the almost full oxidation of the NPs during purification and handling. Reduction of Fe(III) into Fe(II) occurs before the reduction of Ni(II) into Ni(0), which is significant only above 360°C, and slightly precedes the reduction of Fe(II) into Fe(0) which starts at 400°C. Even after 6 h at 530°C, the temperature limit of the set-up (Figure SI 13), more than 70% of Fe remains in the +II oxidation state.

The samples were then brought back to r.t. Unfortunately micro-leaks of air inside the reactor at the end of the cooling precluded any EXAFS analysis of the reduced NPs at r.t. Next,

the samples were exposed to air for a few hours, and XAS data collected from these reoxidized nanomaterials. Comparison of the XANES spectra (Figure SI 15) at the initial, reduced and reoxidized states of the nanomaterials already suggests that Fe is more affected, but that the extent of oxidation is not as pronounced as at the initial state (in accordance with a shorter time of air exposure than during preparation and subsequent storage of the NiFe-S-Ox nanomaterials). MCR-ALS analysis (Table 2) confirms that the re-oxidation of Fe is more pronounced than the one of Ni (65% Fe(III) vs 28% Ni(II) in Ni₂Fe₁-S-Ox, 80% Fe(III) vs 42% Ni(II) in Ni₁Fe₁-S-Ox and 94% Fe(III) vs 63% Ni(II) in Ni₁Fe₉-S-Ox), and indicates that a reduced Ni rich fcc core is preserved for the nanomaterials of Ni/Fe 2/1 and 1/1 compositions while a much smaller reduced core is observed for the Ni₁Fe₉ composition. For the two Ni rich systems, the EXAFS data could be satisfactorily fitted (Fig SI 16-17 and Table 2), and results are in accordance with the MCR-ALS analysis. In each case, the local environment around Ni comprised 2 O only ($R = 2.02 \pm 0.03$ Å) and 8 first metallic neighbours ($R = 2.51 \pm 0.01$ Å) (as indicated above, the best fit was obtained with Ni neighbours only, but the presence of Fe atoms as well cannot be excluded). Contrarily, the local environment around Fe comprised a first shell of O atoms (*ca.* 4 at $R = 1.93 \pm 0.05$ Å), a second shell containing a lower number of metallic neighbours than Ni (4 to 5 at *ca.* 2.53 ± 0.04 Å), and Fe ions from the oxidic shell (1 at *ca.* 3.02 ± 0.1 Å).

Table 2. Structural parameters determined from the EXAFS analysis of the spectra recorded at r.t. at the Ni K edge ($E_0 = 8340 \pm 2$ eV, $S_0^2 = 0.77$) and Fe K edge ($E_0 = 7120 \pm 4$ eV, $S_0^2 = 0.72$) after reduction and re-exposure to air, and results from MCR-ALS analysis.

	Backscatterer	N	σ^2 (\AA^2) $\times 10^3$	R (\AA)
Ni K edge				
Ni2Fe1-S-Ox	O	2.1 ± 0.6	9 ± 2	2.02 ± 0.03
	Ni	8 ± 2	9 ± 2	2.51 ± 0.01
	<i>r-factor</i> = 0.01670, $\chi^2 = 1644$, $N_{ind} = 10$, $N_{var} = 6$			
MCR-ALS analysis : 28% Ni(II), 72% Ni(0) fcc				
Ni1Fe1-S-Ox	O	2.3 ± 0.7	9 ± 2	2.01 ± 0.03
	Ni	8 ± 2	9 ± 2	2.51 ± 0.01
	<i>r-factor</i> = 0.01908, $\chi^2 = 2088$, $N_{ind} = 10$, $N_{var} = 6$			
MCR-ALS analysis : 42% Ni(II), 58% Ni(0) fcc				
Ni1Fe9-S-Ox	MCR-ALS analysis : 63% Ni(II), 37% Ni(0)			
Fe K-edge				
Ni2Fe1-S-Ox	O	3 ± 1	7 ± 4	1.92 ± 0.05
	Ni	5 ± 3	7 ± 4	2.52 ± 0.04
	Fe	1 ± 1	7 ± 4	3.0 ± 0.1
<i>r-factor</i> = 0.01463, $\chi^2 = 1378$, $N_{ind} = 9$, $N_{var} = 8$				
MCR-ALS analysis : 65% Fe(III), 35% Fe(0) fcc				
Ni1Fe1-S-Ox	O	4 ± 2	8 ± 4	1.95 ± 0.04
	Ni	4 ± 2	8 ± 4	2.54 ± 0.03
	Fe	1 ± 1	8 ± 4	3.04 ± 0.08
<i>r-factor</i> = 0.01538, $\chi^2 = 3838$, $N_{ind} = 9$, $N_{var} = 8$				
MCR-ALS analysis : 80% Fe(III), 20% Fe(0) fcc				
Ni1Fe9-S-Ox	MCR-ALS analysis : 94% Fe(III), 06% Fe(0)			

N: Coordination number; σ : Debye-Waller factor; R: Distance between absorbing atom and neighbours; *r-factor*: reliability factor, which measures the relative misfit with respect to the data; χ^2 : reduced chi-square, which takes into account the uncertainty level in the data, as well as the number of free parameters allowed to vary in the fit. N_{ind} : number of independent variables. N_{var} : number of variables used for the fit. Simulations were done over Δk range = 3.5–11.0 \AA^{-1} for Fe, 3.2–11.5 \AA^{-1} for Ni, and $\Delta R = 1$ –3.4 \AA

Discussion

As already observed,^{29–31} the organometallic synthesis of the NiFe NPs led to populations of NPs with very small mean sizes (< 3.5 nm) that were preserved upon deposition onto silica. When all purification steps were carried out in inert conditions and despite the difficulty to remove water from silica and the presence of reactive surface OH groups, no oxidation of the NPs could be detected by WAXS. This indicates that if any, the oxide formed would be amorphous and limited to the very surface of the NPs. This is worth mentioning especially for Ni1Fe9-S which is composed of NPs of only 1.6 nm and with a high content of the oxophilic Fe element. The strong similarity between the structural features of Ni2Fe1-S and Ni1Fe1-S, suggests the same distribution of the two elements in the NPs, independently of their composition and their interaction with the silica: a fcc core enriched in Ni and a polytetrahedral shell enriched in Fe. Comparison of the NiFe-S to their oxidized counterparts gives further indirect proof of this gradient of composition in the NPs as a fcc Ni rich contribution persists in the oxidized samples, while iron is almost fully oxidized. This

preferential location of Fe at the surface of the NPs has already been observed for NiFe nanocatalysts prepared by DPU and attributed to the faster reduction of Ni in comparison with Fe. The same reason can be evoked here as the Ni(COD)₂ complex reacts faster with hydrogen than [Fe(N(SiMe₃)₂)₂]₂. Contrarily, for the Fe-rich sample Ni1Fe9-S, a NiFe alloy of polytetrahedral atomic packing, based on the formerly described Fe polytetrahedral structure,²⁶ is suspected to form. To the best of our knowledge, this unusual mode of alloying was never reported before, and may be related to the very small size of the NPs and to the low content in Ni.

This first part of the study clearly shows that the organometallic approach can afford catalysts with NPs of well controlled size (very small), chemical order and surface state. Especially, this way to access supported while non-oxidized NPs is of interest for applications in hydrogenation catalysis as it could avoid tedious activation steps to achieve a metallic surface and/or allow working in milder conditions. However, the question of handling and storage of these nanomaterials remains. Given that 1) a reduced number of synthesis steps requiring challenging inert conditions, and 2) the possibility of air storage would increase the catalyst applicability, silica-

supported NPs of the same compositions were prepared in a more straightforward manner, all treatments and storage being done in air (NiFe-S-Ox). In this case, as discussed above, an almost full oxidation of Fe into Fe(III) occurred but depending on composition, a fcc Ni rich core was preserved. The fact that this core is more pronounced in Ni₂Fe₁-S-Ox than in Ni₁Fe₁-S-Ox fits well with the larger Ni(0) content in these samples. Indeed combining ICP-OES and MCR-ALS results indicates 1.6 and 1.2 wt% of Ni(0) in Ni₂Fe₁-S-Ox and Ni₁Fe₁-S-Ox, respectively. We will see below that the persistence of this Ni rich core has a strong influence on the reactivity of these NPs in a reducing atmosphere.

The behaviour of NiFe-S-Ox in reducing conditions (5% H₂ in He) was studied to estimate the degree of metallic phase that could be restored.

Interestingly, for Ni₂Fe₁-S-Ox and Ni₁Fe₁-S-Ox, a first redox event was observed at relatively low temperature (ca. 100°C). It is noteworthy that H₂ consumption by core-shell Ni@FeOx NPs (ca. 10 nm large) onto ceria has been reported to start at ca. 95°C.³² Here however, a control experiment carried out in the absence of H₂ showed the same redox event. It is thus interpreted as the reduction of Fe(III) to Fe(II) by the sole Ni(0) of the fcc Ni rich core of the NPs. Ellingham diagrams^{33,34} are classically used to predict such solid state redox transformations in bulk materials, and sometimes also used as general guidelines at the nanoscale.^{35–37} It is noteworthy that, according to these diagrams, Ni should indeed be able to reduce Fe₂O₃ into Fe₃O₄ but not to reduce any of these oxides, nor FeO, into metallic Fe.

Indeed, the full reduction of Fe(III) into Fe(II) and of Fe(II) into Fe(0) required H₂. But the temperatures/times required for the onset and completion of the Fe(II) to Fe(0) reduction are lower/shorter for the NPs with the highest Ni content, which clearly supports a beneficial role of Ni in this process. As the shell of the NPs (an iron rich oxide) probably presents numerous defects, diffusion of H₂ towards the Ni enriched core should be feasible, thus allowing reduction of Ni(II) into Ni(0), activation of H₂ by Ni, and an acceleration of the reduction of Fe(III/II) as a result. The simultaneous onset of Ni(0) and Fe(0) formation was previously evidenced in the case of a SiO₂-supported Ni₁Fe₁ nanocatalyst prepared by DPU followed by hydrogen reduction.¹⁹ It was demonstrated by *in situ* XAS measurements that after reduction of the Fe(III) present in the initial phyllosilicate phase into Fe(II), further reduction to metallic Fe started only with the onset of the reduction of Ni(II) into Ni(0) (above 350°C). Furthermore, after exposure to air, the study of the reactivation of this nanocatalyst under H₂ also showed the beneficial role of Ni on the reduction of Fe.²⁸ A parallel can be drawn with the benefit of adding NiO to iron oxides in order to ease their reduction, that is documented for bulk^{38,39} and nanomaterials.³² It is supposed that NiO first reduces into Ni, which then catalyzes the reduction of iron oxides,⁴⁰ leading to NiFe alloys with an increasing Fe content upon reduction time. The intermediate formation of the Ni(II) ferrite NiFe₂O₄, easier to reduce than Fe₃O₄,⁴¹ is also mentioned. In the present case, NPs are a few nm large and the presence of this oxide could not be

evidenced nor disproved based on the structural data collected in this study, but the formation of a mixed NiFe oxide is possible.

In the reduced state, the similarity of the local atomic packing at the Ni and Fe K-edges evidenced by XANES (Figure SI 15), and especially the fcc atomic packing evidenced at Fe-K-edge by the MCR-ALS analysis, strongly suggests the formation of a NiFe alloy in the Ni-rich NPs as the fcc structure is expected for the alloy at this temperature in this composition range.⁴² It is noted that if the metallic state can be fully restored for Ni₂Fe₁-S-Ox and Ni₁Fe₁-S-Ox, their reduction does not provide the same chemical order and structure than in Ni₂Fe₁-S and Ni₁Fe₁-S, where a clear core-shell order with a fcc core enriched in Ni and an iron rich polytetrahedral shell was evidenced.

For Ni₁Fe₉-S-Ox, displaying a much higher Fe content, a smaller size, and a high degree of oxidation, the partial pressure of H₂ used in this study was not sufficient to reduce it back into the metallic state. Especially the Fe(II)-Fe(0) step could not be completed even after 7h at 530°C. If a fcc atomic packing is clearly observed at the Ni edge (Figure S15), the environment of Fe differs. This is different from what was observed in the reference Ni₁Fe₉-S nanomaterial (where a polytetrahedral arrangement was evidenced for both elements) but reminiscent of the chemical structure observed in the native Ni₂Fe-S-Ox and Ni₁Fe₁-S-Ox nanomaterials and is explained by the only partial reduction of Fe.

Upon reoxidation (a few hours at r.t.) a metallic alloy core still remains in the NPs. However a longer exposure to air could induce a full oxidation of Fe that may be extracted from the metallic core, leading to a chemical order close to the one observed in the initial NiFe-S-Ox nanomaterials. Interestingly, the morphology of the samples was very close to the initial one (Fig. S1-3 and S18).

The ease of reduction of Ni₂Fe₁-S-Ox and Ni₁Fe₁-S-Ox is a plus for the application envisaged: the hydrogenation of sugars. This reaction was successfully carried out at 70°C and 20 bar H₂,²⁰ without any activation step, which suggests that reduction of the surface oxide layer was also achieved in these conditions. *In situ* XAS measurements are unfortunately not possible in these conditions (triphasic system under pressure and mechanical stirring). In comparison, DPU-prepared NiFe nanocatalysts required an energy consuming activation step for their reduction (700°C; 10% H₂/Ar; 2h) in order to allow the catalytic conversion of furfural and xylose into furfuryl alcohol and xylitol, respectively.^{17,19}

As for the NiFe-S-Ox nanomaterials, reaching the metallic state at mild temperature should limit the diffusion of NPs onto the silica support, their coalescence, and the enlargement of the size distribution. It should also limit the degradation of the stabilizing ligands that remain at the surface of the NP after deposition onto the silica, and that can actually help to control the reactivity and selectivity of the NPs.⁴³ The question of the structure and chemical order resulting from *in situ* reduction of the nanomaterials in the catalytic conditions is however still open and this might have consequences on the reactivity of the nanomaterials.

A comparison of the catalytic activity of NiFe-S and NiFe-S-Ox is underway to try and bring answers on this point.

Experimental

Synthetic procedures.

Materials and methods. All syntheses were carried out using Fisher-Porter bottles, a glove-box (Braun, <1 ppm H₂O, <1 mmol O₂) and Argon-vacuum line techniques. Ar ($\geq 99.999\%$, O₂ : ≤ 2 ppm, H₂O : ≤ 2 ppm, C_nH_m : ≤ 0.5 ppm, CO : ≤ 1 ppm, CO₂ : ≤ 1 ppm) and H₂ ($\geq 99.999\%$, O₂ : ≤ 2 ppm, H₂O : ≤ 2 ppm, C_nH_m : ≤ 0.5 ppm, CO : ≤ 0.5 ppm, CO₂ : ≤ 0.5 ppm) were purchased from Air Liquide. Ni(COD)₂ (98%, Strem Chemicals), [Fe(N(SiMe₃)₂)₂]₂ (Nanomeps) and hexadecylamine (HDA) (98%, Sigma-Aldrich) were used as received. Anisole (99%, Alfa Aesar) was degassed by three freeze-pump-thaw cycles then dried over activated molecular sieves (4Å) to reach a water content below 5 ppm prior use. Pentane was collected from a MBraun solvent purification system (H₂O < 5 ppm) and degassed as above. The silica support (Sipernat-50 – Degussa, 400 m² g⁻¹, 1.4 cm³ g⁻¹) was dried under vacuum in the presence of a P₂O₅ (Sigma-Aldrich, > 98%) trap at 120 °C for 72 h before use.

Synthesis of the silica-supported nanomaterials. Ni₂Fe₁-S, Ni₂Fe₁-S-Ox, Ni₁Fe₁-S and Ni₁Fe₁-S-Ox. The procedure described in ²³ was followed adapting the amount of Ni and Fe precursors at the beginning of the synthesis to match the targeted Ni/Fe ratio, in the presence of HDA as a stabilizer. Briefly, after thoroughly washing the Fisher-Porter bottle with anisole the reactants were introduced with the help of a minimum volume of anisole in the following order: HDA, Ni precursor then Fe precursor. Anisole was then added to reach a total volume of 27 mL. After 30 mn, the reacting medium was pressurised under 3 bar H₂ and heated at 150 °C for 36 h. [Ni₂Fe₁-S : Fe(N(SiMe₃)₂)₂]₂ (297 mg ; 0.394 mmol), Ni[(COD)₂] (434 mg ; 1.58 mmol), HDA (191 mg, 0.790 mmol); Ni₁Fe₁-S : Fe(N(SiMe₃)₂)₂]₂ (424 mg ; 0.563 mmol), Ni[(COD)₂] (310 mg ; 1.13 mmol), HDA (272 mg, 1.13 mmol)]. After cooling down to r.t. and evacuation of H₂, a drop of the solution was deposited on a TEM grid to check the average size of the NPs formed (Ni₂Fe₁: 3.4 ± 0.8 nm; Ni₁Fe₁: 3.1 ± 1.0 nm), then silica (1.36 g for Ni₂Fe₁ and 1.30 g for Ni₁Fe₁, corresponding to a target metal loading of 10wt%) and anisole (ca. 45 mL) were added to the black, homogenous dispersion. After 24h of stirring at r.t., the impregnated silica was collected and washed first with anisole (1 x 25 mL) then with pentane (3 x 30 mL). Two processes have been implemented to separate the silica from the solution. Either, magnetic separation was used at all steps in the glove-box followed by withdrawal of the supernatant *via* a Pasteur pipette leading to NiFe-S “non oxidized” nanomaterials, or centrifugation in air was carried out at each step followed by careful removal of the supernatant leading to NiFe-S-Ox “air exposed” nanomaterials. Both kinds of nanomaterials were then dried under vacuum at 50 °C for 2-3 h and stored respectively in the glove-box or in air before characterizations. Ni₂Fe₁-S: 1.42 g; wt%: Ni(5.2), Fe(2.4). Ni₂Fe₁-S-Ox: 1.53 g; wt%: Ni(4.0), Fe(2.0). Ni₁Fe₁-S: 1.32 g; wt%: Ni(3.8), Fe(3.4). Ni₁Fe₁-S-Ox: 1.33 g; wt%: Ni(3.0), Fe(3.1). **Ni₁Fe₉-S and Ni₂Fe₉-**

S-Ox. The procedure described in ²⁵ was followed introducing the adequate ratio of Ni and Fe precursors. Here hexamethyldisilazane formed *in situ* (or by-products thereof) stabilizes the NPs. The black homogeneous dispersion obtained was analyzed by TEM (1.6 ± 0.4 nm) and treated with silica as above to afford the supported NPs. [Ni₁Fe₉-S: 62.9 mg (0.229 mmol) of Ni(COD)₂, 142 mg (0.188 mmol) of [Fe(N(SiMe₃)₂)₂]₂, 75 mL of mesitylene, 1.40 g of silica plus 30 mL of mesitylene. Recovered: 1.68 g ; wt%: Ni(0.7), Fe(6.3). Ni₁Fe₉-S-Ox: 75.3 mg (0.274mmol) of Ni(COD)₂, 852 mg (1.13 mmol) of [Fe(N(SiMe₃)₂)₂]₂, 86 mL of mesitylene, 1.60 g of silica plus 34 mL of mesitylene. Recovered: 1.86 g; wt%: Ni(0.7), Fe(6.3).

Characterization techniques and methods.

Transmission Electron Microscopy (TEM). TEM images were acquired on a JEOL, JEM-1011 microscope, operating at 100kV, point resolution of 0.45 nm, at “Centre de Microcaractérisation Raimond Castaing”, Toulouse. The samples were prepared by drop-casting the colloidal solution of NPs onto carbon coated copper grids (400 hexagonal mesh). Then the grids were subsequently dried under vacuum at least one night before their introduction into the microscope chamber. Size distributions were obtained via the ImageJ software.

Wide-Angle X-Ray Scattering (WAXS). WAXS measurements were carried out at CEMES - CNRS in Toulouse. The samples were sealed in 1.0 mm (diameter) Lindemann glass capillaries under Argon atmosphere for NiFe-S or in air for NiFe-S-Ox. The X-ray scattering intensity measurements were performed using a dedicated two-axis diffractometer using the molybdenum K α (0.071069 nm) radiation monochromatized by a flat graphite crystal. Radial distribution functions (RDF) were obtained after Fourier transformation of the corrected and reduced data.

X-Ray Absorption Spectroscopy. Time-resolved XAS data were measured in the transmission mode at the ROCK beamline ⁴⁴ using the SOLEIL home-made Quick-EXAFS monochromator equipped with a Si (111) channel-cut crystal and described in ref ⁴⁵. The channel-cut oscillates with a $\pm 1.95^\circ$ amplitude around 14.6° and with a frequency of 2 Hz, allowing simultaneous recording of the Fe (7112 eV) and Ni (8333 eV) K-edge spectra in 250 ms. Successive spectra collected with upward Bragg angles during the *in situ* monitoring of catalysts were merged to improve the signal-to-noise ratio, leading to a time resolution of 5 s per spectrum effectively analyzed. Ionization chambers provided by Ohyo Koken Kogyo Co. Ltd. filled with a 2:1 mixture of N₂ and He were used for measurements. The beam size was 2.5×0.5 mm. Normalization of spectra was performed by using the Python normal_gui graphical interface developed at SOLEIL for the fast handling of Quick-XAS data. The proportions of the different Fe and Ni species were determined by a multivariate data analysis, the MCR-ALS method ^{46–48}. MCR-ALS GUI 2.0 developed by the Tauler group ⁴⁹, and freely available as a Matlab toolbox, was used for MCR-ALS minimization. The EXAFS signal extraction and Fourier transformation of the EXAFS spectra were done

using the Athena graphical interface software⁵⁰. EXAFS fitting of distances, coordination numbers and Debye–Waller factors was performed with the Artemis interface to IFFFIT using least-squares refinements⁵¹, firstly checked on NiO, Ni metallic foil and Fe₂O₃ references. Fourier transformed EXAFS signals are presented without phase correction. The temperature-programmed reduction of the « air exposed » samples was performed using a dedicated cell⁵² connected to the gas-feeding system installed on the ROCK beamline. The cavity of the sample holder (2 mm thick) was filled with the powder catalyst (15 mg) pre-mixed with boron nitride (BN, 15 mg). The *in situ* catalyst reduction was performed by heating the cell from r.t. to 530 °C under a H₂ (5%)/He flow (50 mL min⁻¹) with a heating rate of 5 °C min⁻¹, followed by an isothermal treatment if the reduction was not complete after the heating ramp (7 min for Ni1Fe1-S-Ox, 6 h for Ni1Fe9-S-Ox).

Inductively coupled plasma - Optical emission spectroscopy (ICP-OES). Fe and Ni contents were determined with a PerkinElmer, Optima 2100 DV equipment after digestion of the samples in HCl: HNO₃ (3:1 v/v) mixture and dilution with MilliQ water.

Conclusions

The organometallic approach proved to be a powerful solution synthesis method to access model systems of fully reduced NiFe nanoparticles displaying a very small size (1.6–3.5 nm) and a controlled composition (namely Ni₂Fe₁, Ni₁Fe₁ and Ni₁Fe₉), in mild conditions. As often observed for chemical synthesis routes, these NPs present out of equilibrium chemical structures that rely on their composition, as a result of the different kinetics of decomposition of the two metallic precursors involved. These NiFe nanoparticles were then successfully deposited onto a silica by simple impregnation of the support with the colloidal solution of the preformed NPs, while keeping their initial characteristics. This allowed the study of the impact of the chemical environment (oxidative and then reductive) on the structural evolution of these NPs. Interestingly, the combination of WAXS and *in situ* XAS analysis techniques revealed that a polytetrahedral alloy was obtained for the Fe rich composition, Ni₁Fe₉, which is, to the best of our knowledge rarely reported in the literature. Unsurprisingly given their very small size (1.6 nm) and high iron content, these NPs were fully oxidized when their recovery was carried out in air. As for both Ni₂Fe₁ and Ni₁Fe₁ compositions, a Ni-rich fcc core surrounded by a polytetrahedral shell enriched in Fe was evidenced, and their recovery in air led to the preferential oxidation of the Fe shell while a fcc Ni core persisted. The TPR study of these partially oxidized nanomaterials in diluted H₂, evidenced that the reduced Ni core induced an internal redox event that facilitated the first step of the reduction of the iron oxide shell (Fe(II) → Fe(III)), being a rarely reported phenomenon at nanoscale. Full reduction of the nanomaterials could only be achieved for those that still contained a Ni core, namely Ni₂Fe₁ and Ni₁Fe₁, which emphasizes the importance of the initial core-shell chemical structure. It is worth mentioning that when the

reduced state could be restored a change in the chemical structure of the NPs was observed: instead of a core shell chemical order, the thermodynamically stable fcc alloy was formed. As expected, air exposure of these nanomaterials induced their re-oxidation with a surface segregation of Fe but an alloyed core was still maintained. With the aim of replacing noble metals by abundant ones like Ni and Fe, and given the oxidability of these metals, it is fundamental to determine whether the oxidation state of Ni and Fe is significantly and permanently altered by their exposure to air as this may strongly affect the conditions of handling, storage and application of the catalysts to ensure satisfactory performances and durability. Our study highlights that the use of model systems of silica-supported NiFe nanomaterials may at least partially answer this point. If the question of the structure and chemical order resulting from *in situ* reduction of the nanomaterials in real catalytic conditions is still open, our results afford a proof of concepts as well as interesting perspectives. It should be mentioned that the NiFe systems reported herein proved to be active for the hydrogenation of xylose into xylitol in mild conditions, with a catalytic performance close to that of similar but DPU-prepared NiFe nanocatalysts, and importantly without requiring an energy consuming activation step. This study is beyond the scope of the work reported herein, and will be the object of a future paper.

Author Contributions

Conceptualization – CA, FR, KP ; Data curation – VB ; Formal analysis – EM ; Funding acquisition – EM, KP ; Investigation – EM, FR, CA, JSG, PL ; Project administration – CA, KP ; Resources – VB ; Supervision – CA, KP ; Validation – FR ; Visualization – FR ; Writing – original draft – CA ; Writing – review & editing – CA, EM, FR, RW, KP

Conflicts of interest

There are no conflicts to declare.

Acknowledgements

We thank CNRS, Université de Toulouse Paul-Sabatier, Agence Nationale de la Recherche (ANR- 17-CE07-0022-01: “NobleFreeCat” project, <https://noblefreecat.univ-lille.fr/en/>), Région Occitanie (ALDOCT 000355) and SOLEIL synchrotron (project n°20200224) for the financial support of this project. We thank the beamline ROCK team for setting up Fe and Ni K-edge EXAFS experiments and the Chemistry support Lab at synchrotron SOLEIL, and the “Centre de Microcaractérisation Raymond Castaing” in Toulouse for access to the microscopes and Vincent Colliere for his help in recording TEM images.

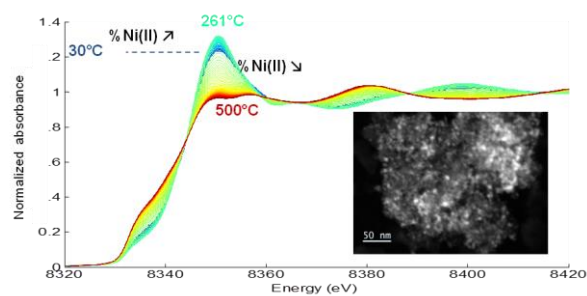
Notes and references

- 1 J. N. Armor, *Catal. Today*, 2011, **163**, 3–9.

- 2 M. Guisnet, *Tech. Ing.*, 2012, 1–12.
- 3 P. Anastas and N. Eghbali, *Chem. Soc. Rev.*, 2010, **39**, 301–312.
- 4 G. Rothenberg, *Catalysis: concepts and green applications*, Wiley-VCH, Weinheim, 2008.
- 5 A. Roucoux and K. Philippot, in *Nanoparticles in Catalysis*, eds. K. Philippot and A. Roucoux, Wiley-VCH, 1st edn., 2021, pp. 1–11.
- 6 I. Fechet, Y. Wang and J. C. Védrine, *Catal. Today*, 2012, **189**, 2–27.
- 7 K. Hill and R. Höfer, in *Green Chemistry Series*, ed. R. Hofer, Royal Society of Chemistry, Cambridge, 2009, pp. 164–166.
- 8 R. A. Sheldon, *J. Mol. Catal. A: Chem.*, 2016, **422**, 3–12.
- 9 A. Corma, S. Iborra and A. Velty, *Chem. Rev.*, 2007, **107**, 2411–2502.
- 10 G. Livesey, *Nutr. Res. Rev.*, 2003, **16**, 163–191.
- 11 Y. Delgado Arcaño, O. D. Valmaña García, D. Mandelli, W. A. Carvalho and L. A. Magalhães Pontes, *Catal. Today*, 2020, **344**, 2–14.
- 12 J. J. Musci, M. Montaña, E. Rodríguez-Castellón, I. D. Lick and M. L. Casella, *Mol. Catal.*, 2020, **495**, 1–12.
- 13 G. Araujo-Barahona, K. Eränen, J. P. Oña, D. Murzin, J. García-Serna and T. Salmi, *Ind. Eng. Chem. Res.*, 2022, **61**, 2734–2747.
- 14 J. Wisniak, M. Hershkowitz, R. Leibowitz and S. Stein, *Ind. Eng. Chem., Prod. Res. Develop.*, 1974, **13**, 75–79.
- 15 G. Chieffi, C. Giordano, M. Antonietti and D. Esposito, *J. Mater. Chem. A*, 2014, **2**, 11591–11596.
- 16 Y. Fu, L. Ding, M. L. Singleton, H. Idrissi and S. Hermans, *Appl. Catal., B*, 2021, **288**, 2–9.
- 17 A. Sadier, D. Shi, A.-S. Mamede, S. Paul, E. Marceau and R. Wojcieszak, *Appl. Catal., B*, 2021, **298**, 1–8.
- 18 A. Sadier, S. Paul, E. Marceau and R. Wojcieszak, *Appl. Catal., B*, 2022, **313**, 1–7.
- 19 D. Shi, Q. Yang, C. Peterson, A.-F. Lamic-Humblot, J.-S. Girardon, A. Griboval-Constant, L. Stievano, M. T. Sougrati, V. Briois, P. A. J. Bagot, R. Wojcieszak, S. Paul and E. Marceau, *Catal. Today*, 2019, **334**, 162–172.
- 20 F. Robert, PhD dissertation, Toulouse 3 Paul Sabatier, 2022.
- 21 C. Amiens, B. Chaudret, D. Ciuculescu-Pradines, V. Collière, K. Fajerwerg, P. Fau, M. Kahn, A. Maisonnat, K. Soulantica and K. Philippot, *New J. Chem.*, 2013, **37**, 3374–3401.
- 22 C. Amiens, D. Ciuculescu-Pradines and K. Philippot, *Coord. Chem. Rev.*, 2016, **308**, 409–432.
- 23 O. Margeat, D. Ciuculescu, P. Lecante, M. Respaud, C. Amiens and B. Chaudret, *Small*, 2007, **3**, 451–458.
- 24 O. Margeat, F. Dumestre, C. Amiens, B. Chaudret, P. Lecante and M. Respaud, *Prog. Solid State Chem.*, 2005, **33**, 71–79.
- 25 L.-M. Lacroix, S. Lachaize, A. Falqui, T. Blon, J. Carrey, M. Respaud, F. Dumestre, C. Amiens, O. Margeat, B. Chaudret, P. Lecante and E. Snoeck, *J. Appl. Phys.*, 2008, **103**, 1–3.
- 26 O. Margeat, M. Respaud, C. Amiens, P. Lecante and B. Chaudret, *Beilstein J. Nanotechnol.*, 2010, **1**, 108–118.
- 27 L. Haim, F. Robert, L. Peres, P. Lecante, K. Philippot, R. Poteau, M. Respaud and C. Amiens, *Nanoscale Adv.*, 2021, **3**, 4471–4481.
- 28 D. Shi, A. Sadier, J.-S. Girardon, A.-S. Mamede, C. Ciotonea, M. Marinova, L. Stievano, M. T. Sougrati, C. La Fontaine, S. Paul, R. Wojcieszak and E. Marceau, *Chem. Catal.*, 2022, <https://doi.org/10.1016/j.checat.2022.04.009>.
- 29 V. Mévellec, A. Nowicki, A. Roucoux, C. Dujardin, P. Granger, E. Payen and K. Philippot, *New J. Chem.*, 2006, **30**, 1214–1219.
- 30 L. Barthe, A. Denicourt-Nowicki, A. Roucoux, K. Philippot, B. Chaudret and M. Hemati, *Catal. Commun.*, 2009, **10**, 1235–1239.
- 31 A. H. Braga, N. J. S. Costa, K. Philippot, R. V. Gonçalves, J. Szanyi and L. M. Rossi, *ChemCatChem*, 2020, **12**, 2967–2976.
- 32 X. Yuan, T. Pu, M. Gu, M. Zhu and J. Xu, *ACS Catal.*, 2021, **11**, 11966–11972.
- 33 H. J. T. Ellingham, *J. Soc. Chem. Ind.*, 1944, **63**, 125–133.
- 34 N. Birks, G. H. Meier and F. S. Pettit, *Introduction to the High Temperature Oxidation of Metals, Second Edition*, Cambridge University Press, 2006.
- 35 I. Narita, *J. Electron Microsc.*, 2006, **55**, 123–127.
- 36 T. Iwamoto and T. Ishigaki, *J. Phys.: Conf. Ser.*, 2013, **441**, 1–5.
- 37 L. Oar-Arteta, T. Wezendonk, X. Sun, F. Kapteijn and J. Gascon, *Mater. Chem. Front.*, 2017, **1**, 1709–1745.
- 38 M. I. Nasr, A. A. Omar, M. H. Khedr and A. A. El-Geassy, *ISIJ Int.*, 1995, **35**, 1043–1049.
- 39 S. Zhou, Y. Wei, B. Peng, B. Li and H. Wang, *J. Alloys Compd.*, 2018, **735**, 365–371.
- 40 V. I. Arjarov, A. K. Varskaya, M. G. Zuravliova and G. I. Chufarov, *Dokl. Akad. Nauk SSSR*, 1952, **87**, 1–49.
- 41 M. Sturzenegger, L. Dsouza, R. Struis and S. Stucki, *Fuel*, 2006, **85**, 1599–1602.
- 42 L. J. Swartzendruber, *J. Phase Equilib.*, 1991, **12**, 288–312.
- 43 L. Lu, S. Zou and B. Fang, *ACS Catal.*, 2021, **11**, 6020–6058.
- 44 V. Briois, C. La Fontaine, S. Belin, L. Barthe, T. Moreno, V. Pinty, A. Carcy, R. Girardot and E. Fonda, *J. Phys.: Conf. Ser.*, 2016, **712**, 1–6.
- 45 E. Fonda, A. Rochet, M. Ribbens, L. Barthe, S. Belin and V. Briois, *J. Synchrotron Rad.*, 2012, **19**, 417–424.
- 46 W. H. Cassinelli, L. Martins, A. R. Passos, S. H. Pulcinelli, C. V. Santilli, A. Rochet and V. Briois, *Catal. Today*, 2014, **229**, 114–122.
- 47 J. Hong, E. Marceau, A. Y. Khodakov, L. Gaberová, A. Griboval-Constant, J.-S. Girardon, C. L. Fontaine and V. Briois, *ACS Catal.*, 2015, **5**, 1273–1282.
- 48 A. Rochet, B. Baubet, V. Moizan, C. Pichon and V. Briois, *CR. Chim.*, 2016, **19**, 1337–1351.
- 49 J. Jaumot, A. de Juan and R. Tauler, *Chemom. Intell. Lab. Syst.*, 2015, **140**, 1–12.
- 50 B. Ravel and M. Newville, *J. Synchrotron Rad.*, 2005, **12**, 537–541.
- 51 M. Newville, *J. Synchrotron Rad.*, 2001, **8**, 322–324.
- 52 C. La Fontaine, L. Barthe, A. Rochet and V. Briois, *Catal. Today*, 2013, **205**, 148–158.

ARTICLE

Table of contents entry



XAS monitoring of the reduction of partially oxidized NiFe nanoparticles evidenced an internal redox phenomenon induced by a residual Ni core, before complete reduction occurred with a change in chemical structure from core-shell to alloy.